



Ambient noise tomography reveals upper crustal structure of Icelandic rifts



Robert G. Green*, Keith F. Priestley, Robert S. White

Bullard Laboratories – Department of Earth Science, University of Cambridge, Madingley Rise, Madingley Road, Cambridge, CB3 0EZ, UK

ARTICLE INFO

Article history:

Received 3 November 2016

Received in revised form 17 February 2017

Accepted 21 February 2017

Available online 17 March 2017

Editor: P. Shearer

Keywords:

Iceland

ambient noise tomography

seismic structure

spreading centre

mid-ocean ridge

ABSTRACT

The structure of oceanic spreading centres and subsurface melt distribution within newly formed crust is largely understood from marine seismic experiments. In Iceland, however, sub-aerial rift elevation allows both accurate surface mapping and the installation of large broadband seismic arrays. We present a study using ambient noise Rayleigh wave tomography to image the volcanic spreading centres across Iceland. Our high resolution model images a continuous band of low seismic velocities, parallelling all three segments of the branched rift in Iceland. The upper 10 km contains strong velocity variations, with shear wave velocities 0.5 km s^{-1} faster in the older non-volcanically active regions compared to the active rifts. Slow velocities correlate very closely with geological surface mapping, with contours of the anomalies parallelling the edges of the neo-volcanic zones. The low-velocity band extends to the full 50 km width of the neo-volcanic zones, demonstrating a significant contrast with the narrow (8 km wide) magmatic zone seen at fast spreading ridges, where the rate of melt supply is similarly high. Within the seismically slow rift band, the lowest velocity cores of the anomalies occur above the centre of the mantle plume under the Vatnajökull icecap, and in the Eastern Volcanic Zone under the central volcano Katla. This suggests localisation of melt accumulation at these specific volcanic centres, demonstrating variability in melt supply into the shallow crust along the rift axis. Shear velocity inversions with depth show that the strongest velocity contrasts are found in the upper 8 km, and show a slight depression in the shear velocity through the mid crust (10–20 km) in the rifts. Our model also shows less intensity to the slow rift anomaly in the Western Volcanic Zone, supporting the notion that rift activity here is decreasing as the ridge jumps to the Eastern Volcanic Zone.

© 2017 The Author(s). Published by Elsevier B.V. This is an open access article under the CC BY license (<http://creativecommons.org/licenses/by/4.0/>).

1. Introduction

1.1. Rifts and plate spreading boundaries

Across the world 20 km^3 of fresh crust is produced every year along the 60,000 km mid-ocean ridge system. Separation of the lithospheric plates drives upwelling and passive decompression melting of the asthenospheric mantle, and the buoyant basaltic melt then segregates and rises to the surface to form new oceanic crust. The new crust is built with a ratio of typically one-third extrusive to two-thirds intrusive products, with melt rising through the crust and delivered to a zone of crustal accretion along the ridge axis (White et al., 1992). Magmatic and extensional features at the spreading axis vary considerably along the mid-ocean ridge system, with the degree of fissuring, and presence of a median rift

valley depending on the thermal state and in turn the spreading rate of the ridge. At all but the slowest spreading ridges, a zone of surface volcanic activity runs down the centre of the crustal accretion zone. Our study concerns the structure of this extensional region at the ridge axis and the volcanic rift zones of the Mid-Atlantic Ridge as it traverses Iceland.

Anomalous low crustal and mantle seismic velocities beneath the ridge axis are a common feature globally. Seismic tomography can be used to study the subsurface pattern of melt delivery in the crust, and the plumbing system which redistributes the melt. These studies, to understand where partial melt resides in the crust and mantle, give insight into how the intrusive and extrusive elements of the crust are formed. On fast spreading ridges such as the East Pacific Rise, a low P-velocity region along the ridge axis extends from 1.2 km below the sea floor, down through the crust and into the mantle at depths greater than 7 km. The region is just 4 km wide at its upper extent and 7–8 km wide at the base of the crust (Dunn et al., 2000), showing that the magmatic system here appears to be focused along a narrow band with a partial melt zone less than 8 km across (Dunn and Forsyth, 2007). The width

* Corresponding author.

E-mail addresses: rgcg3@cam.ac.uk (R.G. Green), kfp10@cam.ac.uk (K.F. Priestley), rsw1@cam.ac.uk (R.S. White).

of the surface eruptive features are also narrow, only 1–2 km wide on fast spreading ridges (Dunn and Forsyth, 2007).

At slower spreading ridges such as the Mid-Atlantic Ridge at 35°N, low velocities are seen only in the mid-to-lower crust (Hooff et al., 2000; Dunn et al., 2005), and in contrast to fast ridges, the formation of new crust is argued to occur over the entire width of the axial valley, which can be up to 40 km wide (Dunn and Forsyth, 2007; Barclay et al., 1998). The seismic crustal structure along the axis is laterally variable (Dunn et al., 2005; Barclay et al., 1998), with melt supply focused at the centre of the segments and with less magmatic activity at the segment bounding tectonic offsets.

1.2. Iceland – a spreading ridge above a mantle plume

The focus of this ambient noise tomography study is to image the upper crustal structure of the spreading ridge in Iceland, which is the only mature oceanic spreading ridge of the entire mid-ocean ridge system found above sea level. While the Mid-Atlantic Ridge spreads slowly here at 18.5 mm a^{-1} , it is not a normal slow spreading ridge, and the seismic structure shows significant differences. The island itself is the product of hotspot volcanism and lies at the centre of a broad 2000 km wide, 3 km high topographic swell, which is believed to be due to the presence of a convective plume in the underlying mantle. The plume hypothesis is supported by the topographic and geoid anomaly (White and McKenzie, 1989), a crustal thickness increase of up to 40 km (Darbyshire et al., 2000a), and by geochemical anomalies in the erupted products along the ridge (White et al., 1992; Sigvaldason et al., 1974; Klein and Langmuir, 1987; Shorttle and MacLennan, 2011). There is also widespread seismological evidence, primarily in mantle tomographic models, of a cylindrical low-velocity anomaly in the upper mantle beneath Iceland (Wolfe et al., 1997; Foulger et al., 2001; Allen et al., 2002a; Rickers et al., 2013). As slow seismic anomalies in the mantle are most likely to be due to temperature or the presence of melt, these low velocity bodies are interpreted to represent a hot upwelling plume conduit. The centre of these slow conduits also coincides with the location of maximum crustal thickness (Darbyshire et al., 2000a), and greatest volcanic activity beneath the north-west edge of the Vatnajökull icecap. The region is therefore believed to be the location of the plume centre.

Because the spreading ridge is sub-aerial in Iceland, the ease of access for geophysical, geochemical and geological methods allows the architecture and crustal structure of rifts to be studied easily. As it comes on land, the Mid-Atlantic spreading centre broadly separates into three identifiable branches or neo-volcanic zones, containing the erupted products of recent magmatic activity. These are known as the northern, western and eastern volcanic zones (NVZ, WVZ, EVZ – Fig. 1). A ridge jump is currently in progress from the WVZ to the EVZ (Hardarson et al., 1997). Within the neo-volcanic zones, the record of Holocene extension is mapped by the distribution of surface fractures and faults, which define distinct fissure swarms. These fissure swarms are each associated with a central volcano, and form the individual oceanic spreading centres of the ridge (Fig. 1 – beige strips). The extension direction in Iceland is at an azimuth of 106° with a full spreading rate of 18.5 mm a^{-1} (MORVEL) (DeMets et al., 2010), defining it as a relatively slow spreading ridge. However, the high magma supply at this hotspot, which is manifest in greater crustal thicknesses than the normal oceanic 7 km (White et al., 1992), means that the crustal spreading centres bear greater similarities to those on fast spreading ridges. No continuous axial melt lens is present, as is found at the East Pacific Rise, but several studies of Icelandic central volcanoes have found evidence of significant shallow magma storage regions (Gudmundsson et al., 1994; Alfaro et al., 2007;

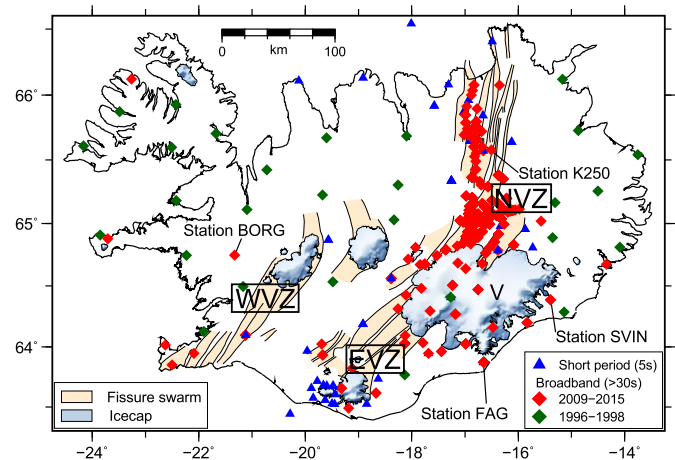


Fig. 1. Icelandic rift systems and seismic station coverage. Icelandic fissure swarms in beige make up the 3 rift zones; the northern, eastern and western volcanic zones (NVZ, EVZ, WVZ). Red diamonds are broadband seismometers from the ongoing Cambridge experiment (plus additional IMO and IMAGE stations). Green diamonds show HOTSPOT broadband stations, blue triangles mark short period seismometers. Ice cover is blue–white. Vatnajökull region labelled V. (For interpretation of the references to colour in this figure legend, the reader is referred to the web version of this article.)

Einarsson, 1978; Brandsdóttir and Menke, 1992; Brandsdóttir et al., 1997; Schuler et al., 2015; Greenfield et al., 2016).

1.3. Crustal seismic structure of a spreading ridge above a mantle plume

Previous studies imaging the Icelandic seismic structure as a whole (Allen et al., 2002b; Li and Detrick, 2006) have frequently resolved a circular low velocity region beneath the centre of Iceland in the lower crust and uppermost mantle. This circular anomaly corresponds to the thickest crust in central-eastern Iceland, and lies within the 200 km wide cylindrical plume conduit anomaly in the underlying mantle (Wolfe et al., 1997; Allen et al., 2002a; Rickers et al., 2013). This lower crustal and upper mantle feature therefore perhaps represents a region of enhanced melt production at the plume head in the upper mantle, and an overlying magmatic plumbing system for transport of melt into the crust in central Iceland.

At shallow crustal levels, Allen et al. (2002b) found that the deeper circular anomaly in the shear wave velocities became a broader feature, elongated along the azimuth of the active rift zones in the mid-to-upper crust. Faster velocities were found in the older Tertiary crust in the far east and west of Iceland. The shape of the anomaly however, did not appear to correlate closely with the boundaries of the rift, though this is unsurprising due to the long wavelengths used ($>40 \text{ km}$). Ambient noise Rayleigh wave observations, at periods down to 4 s, also showed a circular pattern of slow Rayleigh wave group velocities in the centre of Iceland, and faster velocities on the margins (Gudmundsson et al., 2007; Harmon and Rychert, 2016). While the ambient noise measurements extended the observations to shorter wavelengths, the available station distribution limited any discernable increase in resolution. It has therefore remained unclear whether we simply lack the resolution to observe an upper crustal low-velocity signature related to the rift structure at the surface, or whether there is indeed a circular velocity anomaly similar to the circular crustal thickness anomaly.

Here we use an amalgamation of archive and recent seismic datasets to obtain inter-station Rayleigh wave group dispersion curves extracted from ambient seismic noise. We then use a pure ray path approximation and invert path-averaged inter-station group velocities to construct a high resolution velocity model of the mid-to-upper crust across Iceland. The image reveals

an oceanic rift with a focussed and continuous plumbing system feeding all three volcanic rift zones of the plate boundary in Iceland.

2. Methods

2.1. Seismic data

This multi-network ambient noise tomography study uses continuous broadband seismic data from a total of 232 (non-simultaneous) seismic stations across Iceland (Fig. 1). 144 stations are part of an ongoing deployment in central and east Iceland, operated by the University of Cambridge and University of Iceland, and this array is augmented by 48 permanent sites from the monitoring network of the Icelandic Meteorological Office (IMO), and 3 sites from the IMAGE project Reykjanes Ridge experiment. To supplement this, additional archive data from a summer deployment at Eyjafjallajökull volcano and the HOTSPOT experiment of 1996–98 (Allen et al., 2002b) were collated and reprocessed to extend coverage to the margins of Iceland. The backbone of HOTSPOT stations complements the dense rift coverage from the Cambridge and IMO networks. Data for all networks was supplemented with records from the permanent Global Seismic Network station BORG.

The sensors used are predominantly broadband (>60 s–100 Hz) or semi-broadband (30 s–100 Hz) seismometers, with the exception of a minor number of Lennartz 5 s instruments, which are used for additional ray paths at shorter periods and are still valuable with careful quality control (Section 2.4).

2.2. Ambient noise analysis

Ambient noise analysis involves the cross-correlation of long term seismic noise to reconstruct a Noise Correlation function (NCF) which is an estimate of the earth response between two stations. Wavespeed observations, most commonly surface wave dispersion, are then measured for inter-station NCFs and used to determine tomographic velocity maps. Following the earliest verifications of this method (Shapiro et al., 2005; Shapiro and Campillo, 2004), numerous tomographic studies have increasingly developed and refined the technique to improve signal reconstruction. Our methods presented here are similar to those laid out in Bensen et al. (2007) and we also apply a careful quality control procedure to account for the varied instrumentation in our assemblage of datasets and the seasonal noise variation in Iceland.

Continuous vertical component records at 1 Hz sampling rate were split into day-long records, and then demeaned, detrended and tapered and the instrument response was removed to displacement. The mean station pair data record length was 390 days, with 755 pairs having data records longer than 2 yr. Prior to the deconvolution a high pass filter (tapering from 50–60 s) was applied to remove signals which are beyond the period range usable with station separations in Iceland. For data from short period instruments (Lennartz 5 s) the high-pass filter taper was 11–20 s. No additional high-pass filter was applied for sensors with an intermediate frequency response (30 s–100 Hz), in order to maximise the number of available paths with long period observations. Instead, a careful quality control procedure (described in Section 2.4) has been developed. This rejects surface wave information at long periods if the signal quality is not sufficiently high in the resultant Noise Correlation Functions. We follow the pre-processing methods of Bensen et al. (2007), and then cross-correlate in the frequency domain to yield a two-sided Noise Correlation Function (NCF). For all 12,878 station pairs, day files are cross-correlated independently and then stacked to improve the signal-to-noise ratio (SNR) (Fig. 2).

The final stacked NCFs have a high SNR and display a clear Rayleigh wave packet, with a $\sim 3 \text{ km s}^{-1}$ move out on record sections (Fig. 2c). The NCFs typically show a strong asymmetry, which is the result of the anisotropic distribution of noise sources around Iceland, so we take the symmetric average of the two-sided correlation functions (see Section 2.3). Rayleigh wave dispersion of the averaged NCF is then measured using an automated Frequency Time Analysis (FTAN) (Dziewonski et al., 1969; Levshin and Ritzwoller, 2001). The Rayleigh wave group velocity dispersion is measured for all available 12,878 station pairings.

2.3. Noise variability and asymmetry

The spectral content of the seismic noise wavefield varies daily in Iceland, with dominant energy in the secondary microseism band, peaking at a period of 7.5 s (0.14 Hz). The noise wavefield also fluctuates seasonally, showing greater power in the frequency bands of the oceanic microseism during the winter (Fig. 3). This variability is attributed to increased storm intensity in the North Atlantic, as the azimuthal analysis of asymmetric Noise Correlation Functions (Supplementary Fig. S2) shows a dominant surface wave source originating from the south-west of Iceland, which is stable in azimuth through the seasons.

Given the asymmetry of the noise distribution, we scrutinised the reliability of dispersion measurements from both sides of asymmetric NCFs (Supplementary Fig. S3). This confirmed that using the average of the two-sided correlation function provides an appropriate solution to their asymmetry.

2.4. Quality control and temporal repeatability of dispersion curves

Due to the seasonal variability of the noise conditions we assess the temporal reliability of dispersion measurements from the NCFs. As an indicator of the reliability we assess the repeatability of the Rayleigh waves, as any temporal variation in the dispersion curves can be used to quantify uncertainties in the group velocity measurements. The strength of the noise in Iceland is important for this as it allows rapid extraction of a surface wave Green's Function, using stacks of only few months of data.

For each station pair we generate uncertainty correlation functions by stacking day cross-correlations in sliding 3-month windows with a 1-month shift. The long term NCF stack of all available days is used as the measurement waveform, while the variability of the dispersion curves from the uncertainty NCFs (3-month stacks) are used to quantify uncertainty in the group velocity at each period. Several criteria are considered for the selection of a reliable dispersion measurement. First, we define a maximum Rayleigh wave period for each station pair, based on the inter-station separation. Observations are rejected if there are fewer than three complete wavelengths separating the two stations. We then reject station pairs with a broadband SNR of less than 15 for the long term NCF. This reduces the available station pairings to 5925 paths.

The frequency dependent SNR (spectral SNR) is also used to define the period band over which dispersion measurements are accepted. We require the longest period of the dispersion to show a spectral SNR of 7, such that the Rayleigh wave is sufficiently well emerged in the narrow bandpass filters (demonstration in Fig. 4). If the spectral SNR at the separation defined maximum period is below 7, then the maximum observation period is reduced until the SNR exceeds this value (Fig. 4f). This stage is vital for removing observations at longer periods where the frequency response or internal noise level of the seismometer means that the Rayleigh wave signal is not clearly defined. Using this analysis allows the inclusion of data from a variety of instrument types as the long wavelength signals are rejected for data from short-period seismometers.

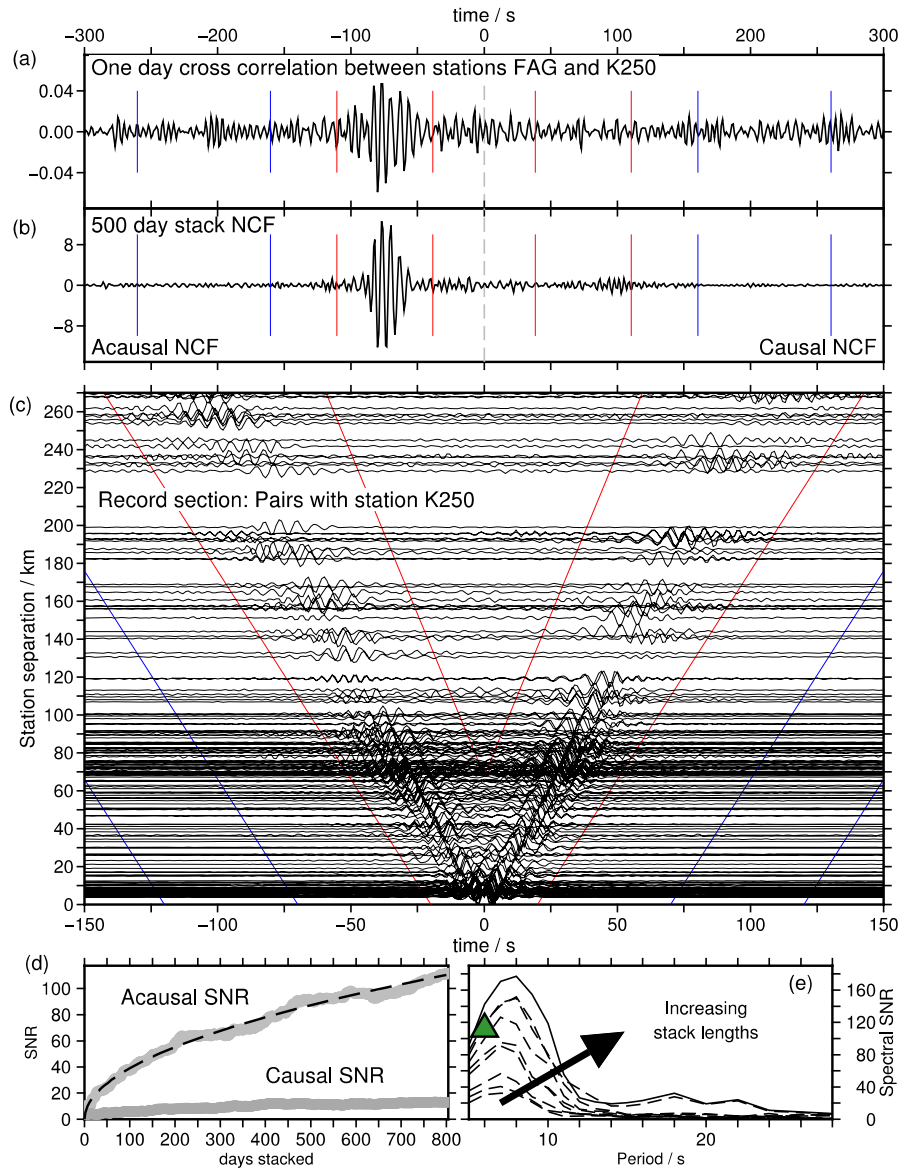


Fig. 2. Extraction of Rayleigh waves. (a) 1-day NCF. (b) 500-day stacked NCF for the same station pair. (c) Record section for pairs with station K250. Red lines show signal window and blue lines show noise window for SNR calculations. (d) SNR emergence with length of stack. (e) Spectral SNR for stacks of 30, 60, 100, 200, 300, 400, 500, 600 and 800 days. Green triangle marks the broadband SNR. (For interpretation of the references to colour in this figure legend, the reader is referred to the web version of this article.)

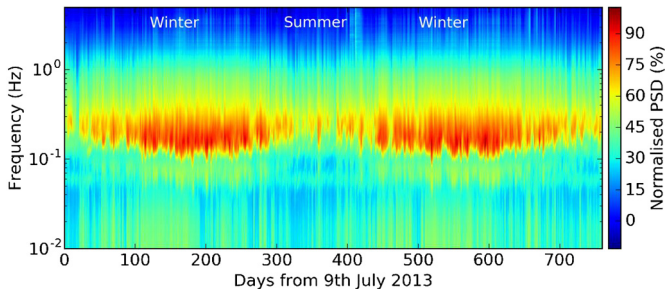


Fig. 3. Seasonal noise variation in spectrogram of station SVIN. (See Fig. 1 for location.) The magnitude and frequency content of the ambient noise wavefield varies seasonally. During the winter the oceanic microseisms are stronger, while the high frequency limit of the local noise shows less seasonal variability.

Uncertainty stacks with a broadband SNR greater than 10 are then used to quantify velocity uncertainties for the remaining observations. For each observation period if there is a minimum of

4 uncertainty measurements then the error is defined as the standard deviation of all values. A minimum for the error is set as 0.01 km s⁻¹ and in the absence of an uncertainty a default error of 0.05 km s⁻¹ is assigned.

2.5. Group velocity tomography

The data used for surface wave tomography consists of group travel times between station pairs, approximated as rays following the great circle paths. A clustering procedure is also applied to remove redundant repeated ray paths (Fig. S4). In this ray-path approximation travel time anomalies are attributed to the geometrical ray path, neglecting sensitivity to structure which is off the ray-path. The study region was parameterised with a 2-D mesh of triangular elements encompassing all stations. A node spacing of 0.1° latitude and 0.2° longitude (~10 by 10 km) is used across the majority of Iceland, though a finer grid is embedded within this, covering the Northern Volcanic Zone and the Vatnajökull ice cap. Here the high density of stations and ray paths merits a spacing of

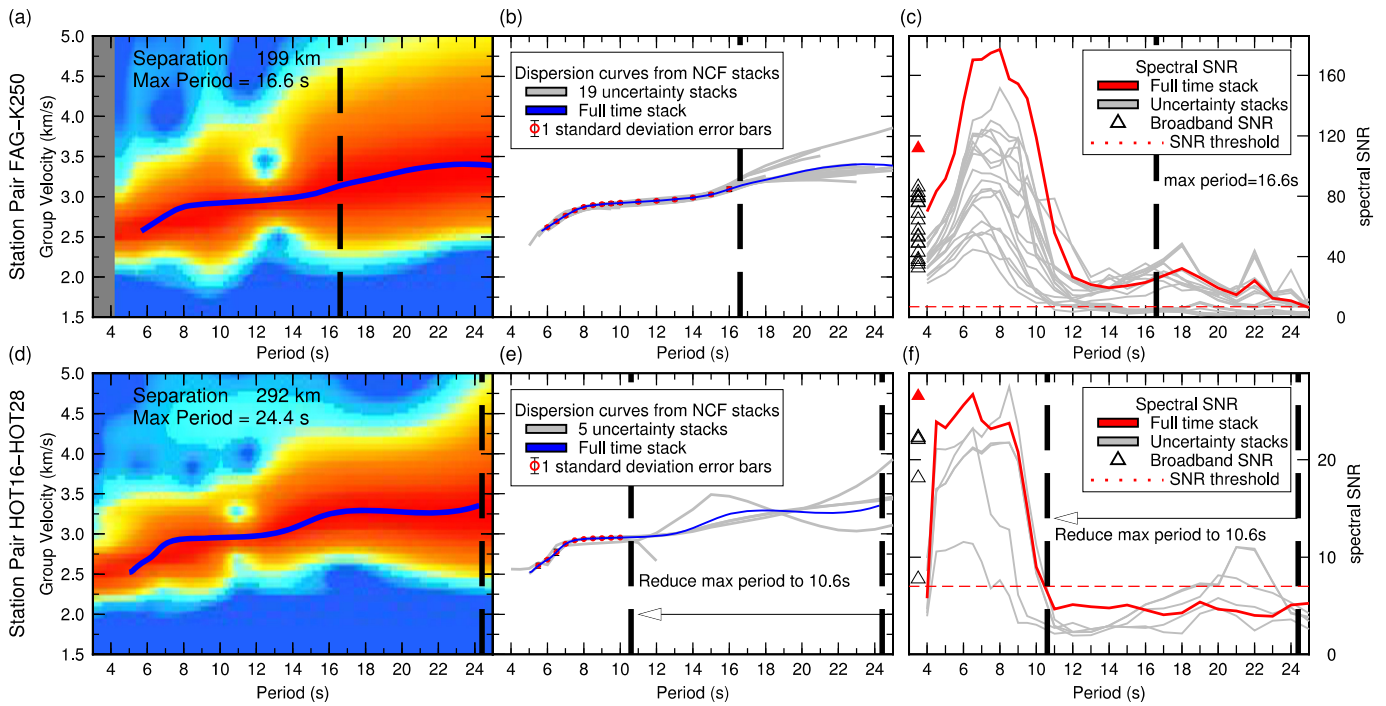


Fig. 4. Quality Control procedure for dispersion measurements at two example station pairs. (a, d) show the FTAN dispersion computed for the long term NCF, and the maximum period calculated for the station pair separation. In (b, e) grey lines display dispersion calculated for all 3-month long uncertainty stacks. (c, f) show the spectral SNR of measurement NCFs (red lines) and 3-month uncertainty NCFs (grey lines). Triangles show the SNR of the broadband NCF. In (c) the spectral SNR at the maximum period (dashed vertical line) is greater than the SNR threshold (dashed horizontal line) so the maximum period is not changed. The dispersion curves (b) below this maximum period are all very similar and the error is estimated with the standard deviation. In (f) the spectral SNR is below the threshold and the maximum period of the measured dispersion has to be reduced until the SNR is above the threshold. Dispersion measurements above the new maximum period (10.6 s) are discarded. (For interpretation of the references to colour in this figure legend, the reader is referred to the web version of this article.)

0.05° latitude and 0.1° longitude (~ 5 by 5 km). Tomographic maps at each period are generated following the method of Mitra et al. (2006). The inversion is stabilised by a smoothing variance matrix, which is constructed by imposing a constraint on the *a priori* standard deviation of the slowness values in the model (σ_{apst}) across a reference distance of 10 km. Decreasing σ_{apst} imposes a stronger smoothing constraint in the variance matrix, reducing the variation in slowness between different nodes in the model. The resulting model thus displays smoother, longer wavelength structure. Velocity errors at each node are computed from the *a posteriori* model variance matrix (Mitra et al., 2006).

We construct Rayleigh wave group velocity maps at periods between 4–25 s (Supplementary Fig. S5). The input data amounts to 25,147 travel time paths. Ray-path coverage is best at 6–8 s period, and is good from 5–16 s. For the data set as a whole, we don't observe a strong azimuthal anisotropy signal (see Supplementary Fig. 8). However, azimuthal anisotropy of varying orientation might still be present locally. Given the good azimuthal coverage of ray paths that we have for most parts of our model, the effects of anisotropy should be averaged out in our inversion. However, azimuthal anisotropy is a possible target for future surface wave studies.

The inversion was performed using a range of values for the smoothing parameter σ_{apst} , varied between 0.01 and 0.5 s km^{-1} . The choice of an σ_{apst} of 0.06 s km^{-1} was made subjectively using the overall misfit, physical reasonability and model error across the well sampled regions. The position of the chosen smoothing is indicated on Supplementary Fig. S6 of the trade-off between misfit and smoothing. The resulting model has a 0.14 km s^{-1} error contour which is a good fit to the ray coverage, and is used to mask regions in the model which are not constrained by the data. For periods of 17 s and greater, there are too few ray paths, with insufficient coverage to constrain a tomographic map with acceptable

errors. Group velocities at these longer periods are still used from some paths for shear velocity inversions in Section 2.7.

2.6. Synthetic recovery tests

Synthetic checkerboard tests illustrate where velocity anomalies can be successfully resolved. A synthetic model is parameterised with alternating blocks of high and low velocities of 4 and 2.5 km s^{-1} (Fig. 5). Using identical ray-paths to those available for the real data at each period (Fig. 6), we calculate the travel times for each path through the synthetic velocity model, and apply a random Gaussian error with variance $\pm 0.05 \text{ km s}^{-1}$. The synthetic travel time data is then inverted using the same tomographic inversion. This is performed for block sizes of 40, 60 and 100 km.

2.7. Inversion for shear wave velocity

To invert for shear wave velocity structure, group velocity maps are further smoothed using a median filter onto a coarser grid of 0.2° latitude and 0.5° longitude spacing. Dispersion curves are then extracted from the suite of group velocity maps between 5 and 16 s period, and inverted for the 1D shear velocity structure using a linearised iterative inversion (*surf96* – Herrmann and Ammon, 2004).

The dispersion curves in all areas exhibit a reduced or even negative dispersion gradient between 9.0–12.0 s period. For some dispersion curves the linear inversion does not successfully converge, such that the modelled and observed data have a visually poor fit. We therefore use a two-stage inversion procedure. We first invert for a structure which fits the short period dispersion data between 4.5–11.0 s. The iterative inversion is allowed to run for 40 iterations, which is sufficient for the model to converge and achieve a good fit to the short-period data. When inverting group

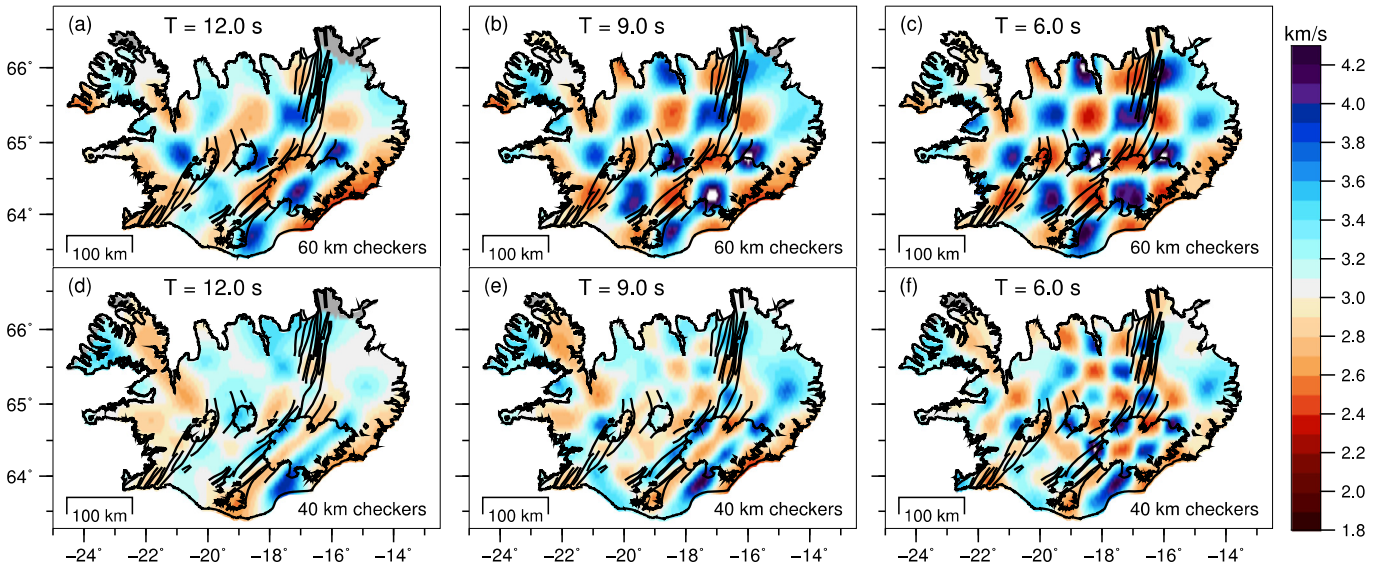


Fig. 5. Synthetic recovery maps at periods of 12, 9 and 6 s for 60 km (a–c) and 40 km (d–f) wide checker squares. Original input velocities were 2.5 and 4 km s⁻¹.

velocities, density and P-wave velocity (V_p) make only a small contribution to the predicted group velocity compared to S-wave velocity (V_s). During the inversion V_p is defined using a linear relation from V_s as in Allen et al. (2002b). The ratio of density to V_s , as set from a density of 2920 kg m⁻³ at the initial V_s , is kept constant through all iterations. The shear velocity model from this first stage is then used as the starting model for the second stage, where all the dispersion data between 4.5 and 16.0 s is used in the inversion.

Due to the large gradients of group velocity as a function of period we used a range of starting velocity models, to determine which features of the crustal structure are reliably constrained. We used half-space starting models, as well as a constant velocity-gradient crust over a half space, and dual layered upper-lower crust over a half space. All models are parameterised into 1 km thick layers. Final shear velocity models shown in Supplementary Fig. S7 are very consistent for the upper ~10 km, but below this depth the variance of the set of recovered models increases dramatically. The period range of reliable tomographic inversions limits dispersion curves to below 16 s period, meaning that the structure deeper than 10 km is poorly constrained. Final shear velocities in the lower crust are dependent on the velocities in the starting model, whereas in the upper crust consistent shear velocity profiles are recovered from a large range of starting models. If future studies could independently identify the correct phase velocity branch of our ambient noise Rayleigh waves, then we may subsequently be able to add phase velocities to the analysis. Adding independent phase velocity control would then improve constraint on the structure to a few kilometres deeper, and the absolute velocities at depth would be more robust.

This lack of constraint at depth is reflected when reconstructing maps of the shear velocity from the individual 1D shear velocity profiles. Below 10 km depth the shear velocities are scattered and highly variable in map view and show little resemblance to either the rift geometry or the tomography maps at 12–16 s period. The variability of the final V_s models at depth (red envelope in Fig. S7) is greater than the lateral heterogeneity in the maps. We therefore present only shear velocity maps of the upper crust, where we obtain a more reliable velocity structure (Fig. 7). Three across-rift sections (Fig. 8) are generated by inverting groups of dispersion observations in 20 km long bins along nearby projection lines.

2.8. Average crustal shear velocity profiles

While the lack of longer period tomographic maps limits the determination of deep shear velocity structure at individual model nodes across Iceland, an average structure can be constrained for broader regions. We construct on-rift and off-rift provinces (Fig. 9) and use the tomographic dispersion velocities in these regions, as well as additional ray-paths from station pairs which are largely restricted to the area of this province. The Rayleigh wave dispersion observations that can be inverted then extend to 24 s, providing better constraints on the average mid-lower crustal structure for these separate tectonic provinces.

3. Results and discussion

3.1. Rift zones and spatial velocity variations

Group velocity maps in Fig. 6 and shear velocity results in Figs. 7–9 present this regional model of crustal velocity structure across Iceland. In Fig. 6, Rayleigh wave propagation velocities are consistently slower across all periods within the volcanic rift zones compared to outside them. By contrast, the regions that are not volcanically active have wavespeeds up to 0.5 km s⁻¹ faster than the rifts, a variation similar to that observed by Allen et al. (2002b). Faster velocities imply a cooler, older and lower porosity crust outside the rifts, discussed further in Section 3.3. The high resolution of our results, however, shows a ridge structure never before observed in such detail in velocity maps. We first discuss the more detailed features of the group velocity maps, before interrogating the smoother properties of the shear velocity structure.

Contours of the slow anomalies on the group velocity maps (Fig. 6 and Supplementary Fig. S5) show excellent correlation with the currently active rifting regions, as defined by the extent of basaltic bedrock younger than 0.7 Ma. At periods greater than 8 s the low-velocity anomalies are continuous along all three branches of ridge, with low velocities linking the western arm of the ridge to the continuous and more active section of the ridge along the Northern and Eastern Volcanic Zones. The spatial resolution of the model improves towards shorter periods, and at less than 9 s the extent of the low-velocity anomalies become more closely correlated with the boundaries of the individual spreading centres on the margins of the neo-volcanic zones. This is especially clear on the edges of the western and eastern neo-volcanic zones, defining

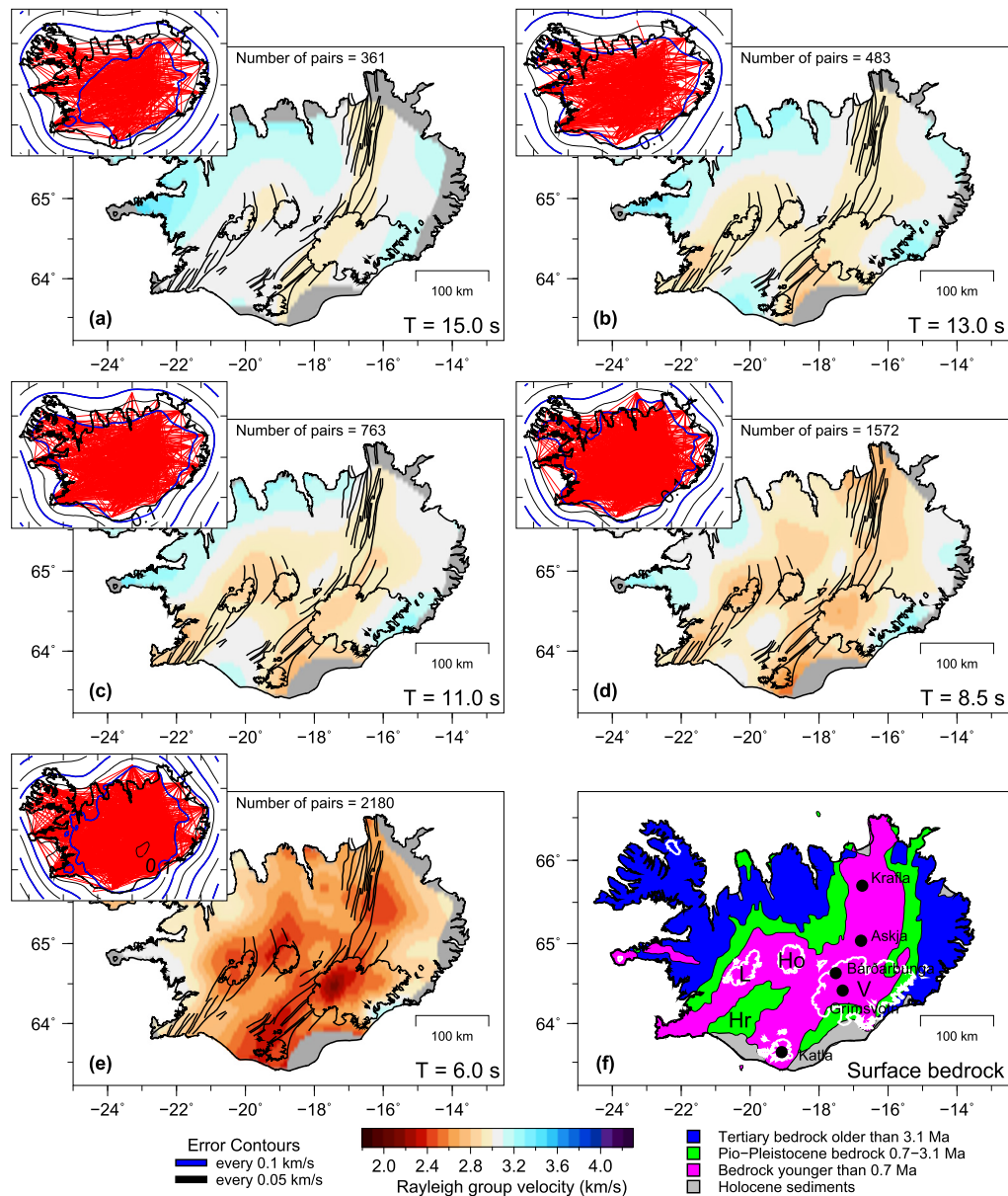


Fig. 6. Rayleigh wave group velocity maps at 15–6 s period (a–e) and comparison to surface geology (f). Grey regions of the model are unconstrained, clipped at the 0.14 km s^{-1} error contour. Black lines mark the rift systems and ice caps for reference. Inset maps show the ray path distribution as red lines. Blue and black lines display error contours every 0.1 and 0.05 km s^{-1} . The smoothing parameter, σ_{psl} is 0.06 for all maps. (f) shows surface bedrock age, reproduced from Jóhannesson and Saemundsson (1998). Langjökull, Hofsjökull and Vatnajökull are labelled L, Ho, V. Hreppar microplate is labelled Hr. Crust younger than 0.7 Ma in (f) delineates the modern neo-volcanic zones. Major volcanic centres discussed in the text are labelled in (f). (For interpretation of the references to colour in this figure legend, the reader is referred to the web version of this article.)

the boundary with the Hreppar microplate (Fig. 6f). The Hreppar microplate and the older crust in eastern, northern and western Iceland show clearly faster group wavespeeds than the rifts.

Synthetic recovery tests (Fig. 5) suggest that features larger than 60 km are well resolved across all of Iceland, and that in the densely instrumented eastern half of Iceland features of 40 km in size are still resolved. Velocity anomalies associated with the volcanic rift zones are greater than 60 km in lateral extent, so they are likely to be resolved reliably by this data. Their correlation with the surface geology also acts as compelling support for the reliability of the structure.

The rifts in Iceland also display an unusual feature of mid-ocean ridges: two parallel segments that overlap for a distance of greater than 100 km. The shear velocity models (Fig. 7) indicate that despite the lower eruptive activity of the WVZ, the region still has depressed shear velocities. Slow shear velocities extend down

the WVZ to the Reykjanes Ridge, but are less pronounced in the western compared to the eastern rift and do not extend as deep. This agrees with the contrast between the high volcanic activity in the EVZ and the lower Holocene activity in the WVZ. It is a well established theory that the WVZ is a dying rift, with spreading switching to the EVZ, for which our model shows good support. Cross sections of shear wave velocity structure show the same pattern in Fig. 8d, where the slow shear wave velocities in the upper 8 km are stronger for the EVZ than for the WVZ. By comparison in cross section Fig. 8b, which passes through the NVZ, there is only one shallow low shear-velocity feature.

3.2. The 1D shear velocity structure of Iceland

Analysis of the average shear velocity structure in broad on-rift and off-rift provinces is shown in Fig. 9. Here, longer period group

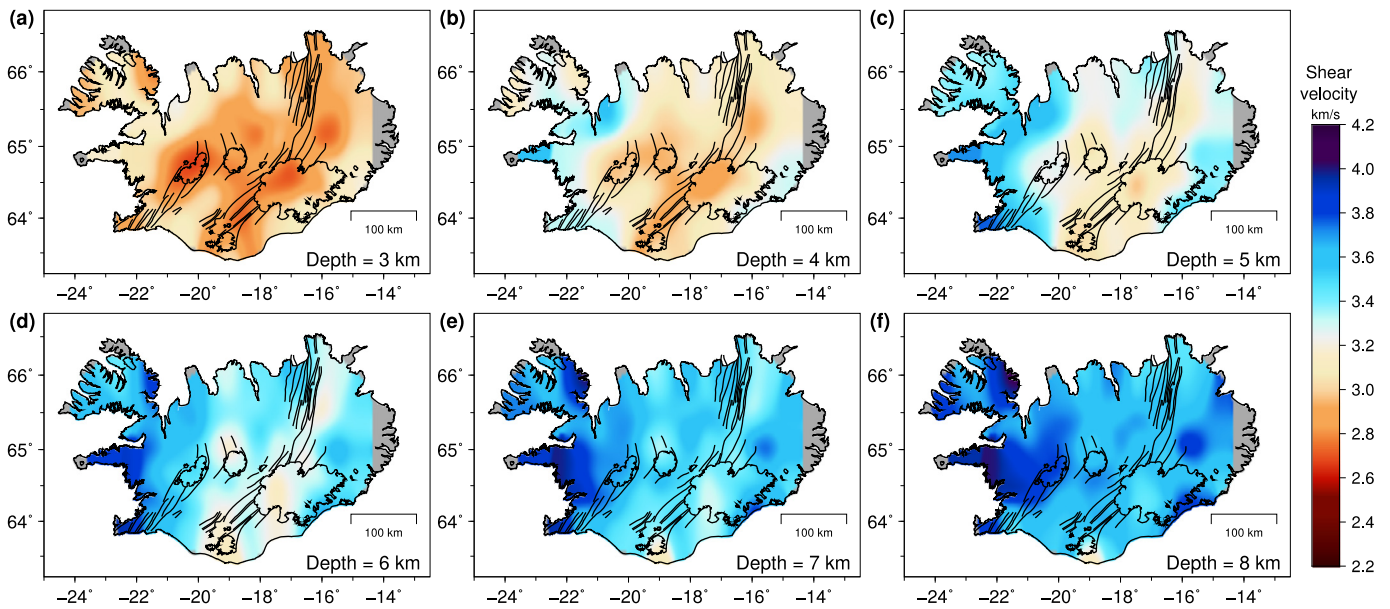


Fig. 7. Shear wave velocity maps in the upper crust at depths of 3 to 8 km. Grey regions of the model are unconstrained. Map features as in Fig. 6. See Fig. S9 for comparison to previously published results.

velocities from nearby ray paths have been added to the group velocities from the tomographic inversions. This improves resolution in the crust down to 20–25 km, but our Rayleigh wave sensitivity does not extend sufficiently deep to speculate on the crust-mantle transition across Iceland.

The shear wave velocity profile with depth of the Icelandic crust shows high velocity-gradients in the upper crust, with the shear velocity at the base of the high gradient layer (8–10 km) reaching around $3.6\text{--}3.8\text{ km s}^{-1}$. In the oceans, this high gradient layer is known as oceanic layer 2, and is typically interpreted as representing upper crustal extrusive igneous products. The high velocity-gradients are inferred to be a result of decreasing fracture density due to the increasing overburden and to the infilling of cracks by secondary mineralisation. We find that this upper crustal layer in Iceland is approximately three times greater than in normal 7 km thick oceanic crust (White et al., 1992). This is consistent with the roughly 3 times increase in the total crustal thickness, maintaining a ratio of one-third extrusives to two-thirds intrusives building the oceanic crust. As displayed in Fig. 9 (along with Fig. 7 and Fig. 8), there is a strong reduction in the shear velocity in the volcanic rift zones, especially within the upper crust (0–10 km). The shear wave velocity is 0.5 km s^{-1} slower in the rift compared to off-axis locations, less than the 2 km s^{-1} reduction seen at the East Pacific Rise (Dunn et al., 2000).

Below 9 km depth the velocity-gradient then decreases dramatically. Shear wave velocity profiles in the mid-crust show very low vertical velocity-gradients, with a much reduced difference between the on-rift and off-rift profiles. The range of the constrained shear velocity envelopes increases with depth. Although the envelope of the off-rift profiles can define a relatively linear velocity gradient between 10 and 20 km depth, the on-rift envelope shows a very slight reduction in the shear wave velocity (0.1 km s^{-1}) between depths of 10–20 km. Forward modelling with a simplified structure confirms that a reduction of velocities in the mid crust derives from fitting the flattening and then increase in the dispersion gradient seen on the dispersion curves in Fig. 9b. This flattening is present in the raw path-averaged dispersion as well as in the local dispersion curves, so this mid-crustal velocity reduction is a noteworthy feature.

3.3. What causes low seismic velocities?

Given that the bulk of Icelandic crust is compositionally homogeneous basalt, the velocity differences reflect variations in the thermal conditions, partial melt content and degree of porosity, fracturing and faulting of the crustal rocks.

The spatial variation we observe in upper crustal velocities appears to be primarily controlled by age. This can be seen by the excellent correlation between the map of surface bedrock (Fig. 6f) and the velocity maps of Fig. 6 and Fig. 7. From Fig. 9a it is evident that these spatial velocity contrasts are concentrated within the upper high-gradient layer of the crust (top 10 km). The same age variation of upper crustal velocities is seen in collations of refraction profiles results in oceanic crust (White et al., 1992). In these, the near-surface compressional velocities are lowest in younger crust, and increase with age of the oceanic crust. However, while velocities increase with age in the high-gradient upper crustal layer, the velocities deeper in the crust do not vary with age. We infer that the spatial variations we see in Iceland are a result of this ageing effect, whereby the higher porosity of younger rifted crust reduces over time through precipitation and mineralisation within pore spaces. The velocity of the shallow fractured crust therefore increases with age. An extrusive origin for the upper crustal layer would explain why the on-rift to off-rift velocity contrast is greatest in this upper layer (Fig. 9a), as only extrusive or shallowly emplaced material will have inherent porosity which can heal and reduce with age. Deeply emplaced cumulates would have no initial porosity, and as is seen in the refraction experiments in the oceans (White et al., 1992) the velocity does not increase significantly with time.

At mid-crustal depths (10–20 km) the slight difference in shear velocities between on-rift and off-rift is not a strong signal, but the flattening of dispersion curves that produces the low-velocity bulge is consistent on both local dispersion and the path-averaged data. This small velocity contrast at depth between on-rift and off-rift could be attributed to melt or to an increased temperature effect. Small quantities of partial melt act to lower the bulk shear modulus, with some experiments (Caricchi et al., 2008) suggesting that to reduce the shear velocity by 0.1 km s^{-1} would require less than 1% partial melt. Temperature could also be important because with depth the pressure and temperature increase have opposite effects

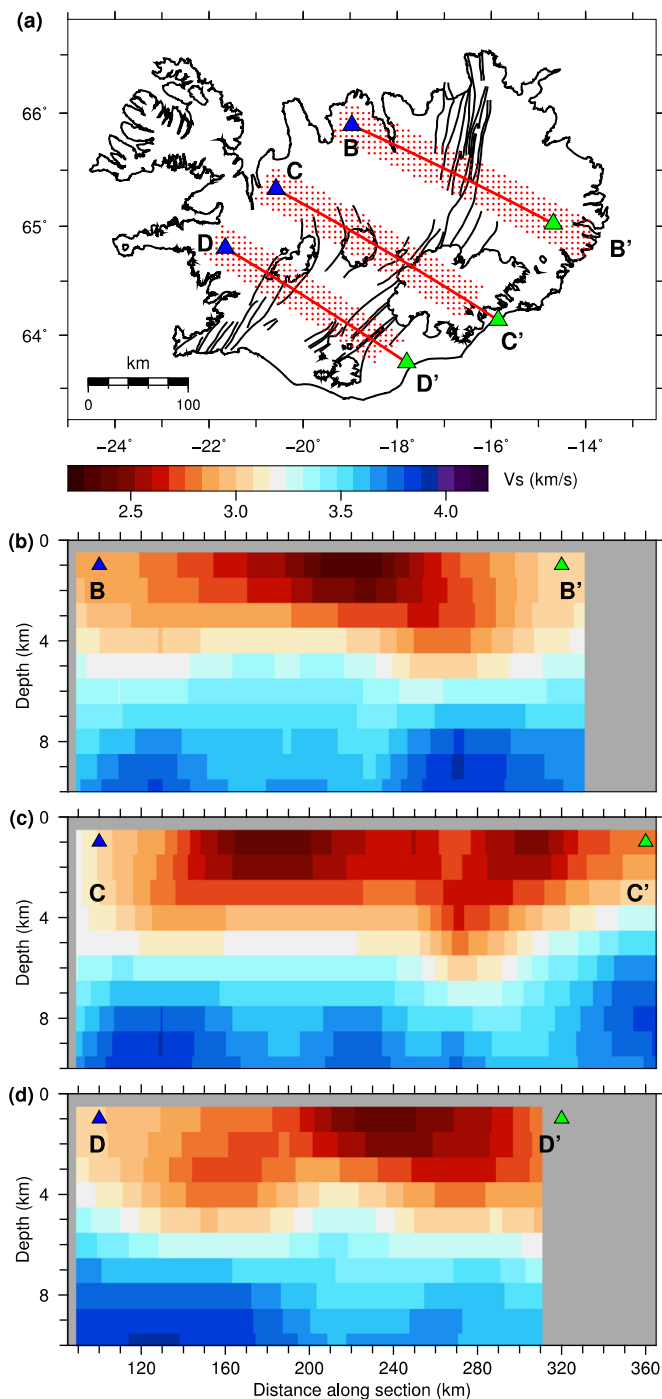


Fig. 8. Cross sections of shear wave velocity structure across rift (b, c, d). (a) Map showing cross section locations, and in red the points from which dispersion data is projected onto the cross sections. Blue and green triangles are reference distance markers. Grey areas are clipped by errors greater than 0.14 km s^{-1} and are unconstrained. (For interpretation of the references to colour in this figure legend, the reader is referred to the web version of this article.)

on the shear velocity. In this thick crust, which must be $>1400^\circ\text{C}$ at its base (Matthews et al., 2016), the high temperatures would mean the shear velocity deviates more when the crust is close to the homologous temperature of basalt. To estimate the velocity perturbation if it were solely the effect of temperature, we have to rely on a limited set of constraints from experiments on basaltic rocks at temperatures and pressures greater than the shallowest few kilometres. While there has been much focus on this problem for mantle compositions, the temperature dependence of shear ve-

locity in basalts has not been studied extensively. Using the shear velocity gradient from the experimental results of Birch (1943) on gabbro at 4.8 kbar (c. 16 km depth), the 0.1 km s^{-1} velocity decrease could be produced by a temperature increase of 200°C .

It is unsurprising that such a small velocity reduction in the oceanic crust of Iceland has not been previously resolved, as the majority of Icelandic crustal studies have been wide-angle refraction experiments. Observing low-velocity zones with refraction studies requires the identification of a clear shadow zone along the receiver line; a task which is notoriously challenging with noisy data in a laterally inhomogeneous crust exhibiting large thickness variations. The compressional velocities constrained by wide-angle experiments are also less sensitive to temperature than are the shear velocities to which Rayleigh waves are sensitive, especially at temperatures close to the solidus, and so it may be that the V_p does not decrease in the mid crust.

3.4. Magmatic centres and very low velocities

Around magmatic centres it is likely that partial melt plays a role in reducing the shear velocity. Within the rifts, the slowest wavespeeds are concentrated along the Eastern Volcanic Zone and the western edge of the Vatnajökull ice cap (Fig. 6 and Fig. 7). These are two regions which experience the highest volcanic activity in Iceland, and the strong cores of the anomalies are centred over the largest volcanic centres in Iceland: Katla, Bárðarbunga and Grímsvötn (locations in Fig. 6f). The high magmatic output of these large volcanic centres (Gudmundsson and Larsen, 2015; Larsen and Gudmundsson, 2015) and the variety of eruptive styles, between effusive basaltic eruptions to caldera forming explosive silicic eruptions, suggests that these volcanic centres must have extensive magmatic plumbing systems and melt storage regions.

The very lowest seismic velocities occur beneath the Bárðarbunga–Grímsvötn volcanic complex, two closely associated sub-glacial volcanoes which have dominated Icelandic volcanism in recent times (Gudmundsson and Larsen, 2015; Larsen and Gudmundsson, 2015). This volcanic complex is also the location where the thickest crust and centre of the mantle plume is believed to be positioned (Wolfe et al., 1997; Foulger et al., 2001; Allen et al., 2002a). At arguably the focus of maximum melt transport into the crust beneath Iceland, it is likely that partial melt plays a role in the strong reduction in shear wave velocity at these large magmatic centres.

Shallow magma storage regions (or ‘magma chambers’ as they are often unfortunately called) have been imaged at both Katla using seismic refraction (Gudmundsson et al., 1994) and Grímsvötn using body wave tomography and shear wave attenuation (Alfaro et al., 2007). Similar observations also constrain melt bodies at Krafla (Einarsson, 1978; Brandsdóttir and Menke, 1992; Brandsdóttir et al., 1997; Schuler et al., 2015) and Askja (Greenfield et al., 2016) central volcanoes in the Northern Volcanic Zone, where seismic velocities are also low. However, these imaged melt bodies are small, less than 5 km in dimension and never more than a few kilometres thick.

The volcanological community is now increasingly agreed that the magmatic plumbing system beneath volcanoes is not characterised by liquid dominated vats of magma. Erupted products of these large volcanoes attest to the existence of liquid-rich layers at some point in time, but the petrological and geochemical evidence is in favour of extensive regions of partially molten rock and crystal mush, which only in some cases accumulate isolated liquid-rich regions.

With this surface wave study the wavelengths of even the shortest period Rayleigh waves are approximately 15 km, so we do not expect to image individual crustal storage reservoirs such as those determined with the refraction and body wave studies men-

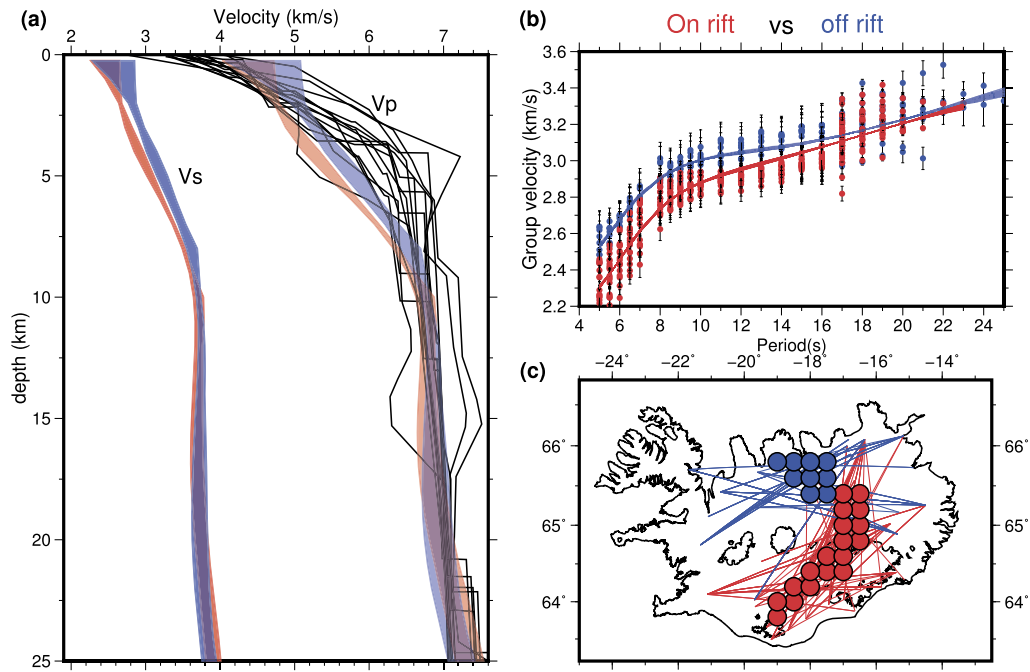


Fig. 9. Shear velocity profiles for on-rift (red) and off-rift (blue) regions of Iceland. (a) Red and blue bands show the envelope of shear velocity resulting from different starting models. V_s results are scaled up with a V_p/V_s relation (described in Section 3.5) to compare with V_p profiles from published refraction experiments in Iceland (Bjarnason et al., 1993; Darbyshire et al., 1998; Menke et al., 1998; Staples et al., 1997). Full inversion results in Fig. S7. (b) displays fit to Rayleigh wave group dispersion results on-rift (red) and off-rift (blue). (c) shows the nodes of the province (coloured circles) and the additionally incorporated inter-station ray paths. (For interpretation of the references to colour in this figure legend, the reader is referred to the web version of this article.)

tioned previously. Instead the velocities we constrain must reflect the effect of partial melt present over a broad region, or of elevated temperatures of the crust beneath these large volcanic centres.

3.5. Comparison with other rifts and mid-ocean ridge segments

The Afar rift in east Africa is another hotspot spreading centre producing basaltic crust, and is spreading at a similar rate to Iceland. There is evidence there and in the Mid Ethiopian Rift for widespread melt, with V_p/V_s ratios approaching 2 (Hammond et al., 2011), elevated conductivity in magnetotelluric experiments, and seismic anisotropy which can be explained by along-rift alignment of vertically oriented melt pockets (Bastow et al., 2010). By contrast in Iceland the current evidence does not support the presence of widespread melt in the crust. Wide-angle refraction experiments repeatedly constrain V_p/V_s as 1.76–1.79 (Brandsdóttir et al., 1997; Bjarnason et al., 1993; Darbyshire et al., 1998; Menke et al., 1996, 1998; Staples et al., 1997) across many areas of Iceland, and only isolated observations of higher V_p/V_s have been made. One such example of 1.88 at a station at Krafla central volcano is probably a local effect following the 1975–84 rifting episode (Darbyshire et al., 2000b). Wadati diagrams from local microseismic studies (Greenfield et al., 2016; Green et al., 2014) also provide path averaged V_p/V_s ratios which always lie in the range 1.76–1.78. We also scaled our shear wave velocity profiles by a V_p/V_s factor to broadly match the P-wave velocity profiles of previous refraction profiles (Fig. 9a). We use the same depth dependent relation as Allen et al. (2002b) whereby the V_p/V_s ratio is 1.78 at the surface, increasing to 1.88 at 25 km depth. These lower V_p/V_s ratios in Iceland and the absence of S-wave attenuation is consistent with low melt-fractions and temperatures that are below the solidus. The difference in the presence of melt across broad areas, implies that the oceanic crust in Iceland has lower melt retention capabilities than the continental crust in Ethiopia, or the young oceanic crust of Afar. In lower density continental crust it may be that the mantle melts find a level of neutral buoyancy, or that continental

crust is remelted. The reason for a difference between Afar is less clear as the crust there is also highly stretched and is approaching oceanic.

The large scale picture of rift seismic structure can be compared to other sections of the mid-ocean ridge system. In our model slow anomalies are continuous along the neo-volcanic zones of the Icelandic ridge system, similar to what is found under fast spreading ridges in the oceans, but unlike the East Pacific Rise (EPR) the low-velocity anomaly in Iceland is a wide feature, not restricted to less than 8 km across. The low velocity region we image extends to the full width of the neo-volcanic zones, some 50 km across. Some of this could be attributed to the characteristic smoothing effect of the tomographic method, but our synthetic testing (Fig. 5) suggests that if the feature were narrower this would be resolved. Hydrothermal circulation and efficient heat removal have been shown to be important in producing the narrow ridge-parallel velocity anomaly on fast spreading ridges like the EPR (Dunn et al., 2000). The broadness of the low-velocity band in Iceland could therefore be interpreted as reflecting depressed hydrothermal circulation compared to the submarine setting of the EPR.

In Iceland the strongest low velocities at Katla and under north-west Vatnajökull may be related to a broad region of partial melt in the plumbing system of these volcanoes. These focus points support the suggestion that melt supply into the crust is concentrated at a few particular points along the neo-volcanic zones. Similar focal points have been observed on submarine segments of the mid-ocean ridge system, for example on the Mid-Atlantic Ridge at 35°N (Dunn et al., 2005) where melt supply peaks in the segment centres and is reduced at the ends. However, in Iceland there is no evidence in crustal thickness variations for any reduced overall supply between focus points. This suggests that lateral flow can then effectively redistribute the focused melt within the volcanic systems, as occurred in the 2014 Bárðarbunga–Holuhraun dyke intrusion.

It seems that Iceland exhibits similarities with both fast and slow spreading ridges. As at fast spreading ridges, where melt in-

flux is rapid, the plumbing system and magmatism is continuous along the ridge axis. This is explained by the high melt supply rates that occur from enhanced melting on this hotspot spreading ridge. However, with lower spreading rates the surface expression of the magmatic zone is wider than on fast ridges, and the ridge parallel low-velocity band which we observe is correspondingly many tens of kilometres wider.

4. Conclusions

We have collected and assimilated a large dataset of continuous broadband seismic data for ambient noise analysis, and implemented a careful quality control procedure to remove poor quality data and to estimate uncertainty in the Rayleigh wave group velocities.

Our high resolution model of the shear velocity structure of the Mid-Atlantic Ridge in Iceland displays an excellent spatial correlation of low seismic velocities within the active rift zones, and faster velocities in the older, cooler, less fractured, non-volcanically-active crust. This image reveals an oceanic rift with a continuous plumbing system feeding all three volcanic rift zones of the plate boundary in Iceland.

Strong cores of the low-velocity anomalies are focussed under Katla and north-west Vatnajökull, and are possibly related to a broad region of partial melt under these large volcanic complexes, suggesting a concentrated delivery of melt into the crust at these locations.

Shear wave velocity profiles of both on-rift and off-rift regions show a high velocity-gradient upper crust of 8–10 km thickness. Below this, shear velocities increase with a lower velocity-gradient, and in the on-rift region the crustal shear velocities are depressed between depths of 10–20 km.

Author contribution statement

All authors contributed to interpretation of data, and to preparation of the manuscript. RGG and RSW collected the data from seismometers deployed in Iceland. Processing and analysis of the seismic data was carried out by RGG.

Acknowledgements

Seismometers were borrowed from the Natural Environment Research Council (NERC) SEIS-UK (loans 968 and 1022). The work was funded by a graduate studentship from the NERC and research grants from the NERC (grants NE/F01140711, NE/M017427/1, NE/H025006/1) and the European Community's Seventh Framework Programme Grant No. 308377 (FUTUREVOLC). We thank Bryndís Brandsdóttir, Sveinbjörn Steinþórsson and all those who assisted with fieldwork in Iceland. Chris Bean (University College Dublin), the British Geological Survey and Icelandic Meteorological Office (IMO) kindly provided additional data from their seismometers in north-east Iceland: data delivery from IMO seismic database 20141124/01 and 20151001/01. We thank Philippe Jousset and IMAGE project for data shared from three stations in south-west Iceland. IMAGE project has received funding from the European Union's Seventh Programme for research, technological development and demonstration under grant agreement number 608553. Stations for this project were provided by the Geophysical Instrument Pool of Potsdam (GFZ). Dept. Earth Sciences, Cambridge contribution number ESC3818.

Appendix A. Supplementary material

Supplementary material related to this article can be found online at <http://dx.doi.org/10.1016/j.epsl.2017.02.039>.

References

- Alfaro, R., Brandsdóttir, B., Rowlands, D.P., White, R.S., Gudmundsson, M.T., 2007. Structure of the Grímsvötn central volcano under the Vatnajökull icecap, Iceland. *Geophys. J. Int.* 168 (2), 863–876.
- Allen, R.M., Nolet, G., Morgan, J., Vogfjörð, K., Bergsson, B., Erlendsson, P., 2002a. Imaging the mantle beneath Iceland using integrated seismological techniques. *J. Geophys. Res.* 107 (B12), 2325.
- Allen, R.M., Nolet, G., Morgan, W.J., Vogfjörð, K., Nettles, M., Ekström, G., et al., 2002b. Plume-driven plumbing and crustal formation in Iceland. *J. Geophys. Res., Solid Earth* 107 (B8), 2163.
- Barclay, A.H., Toomey, D.R., Solomon, S.C., 1998. Seismic structure and crustal magmatism at the Mid-Atlantic Ridge, 35°N. *J. Geophys. Res., Solid Earth* 103 (B8), 17827–17844.
- Bastow, I.D., Pilidou, S., Kendall, J.-M., Stuart, G.W., 2010. Melt-induced seismic anisotropy and magma assisted rifting in Ethiopia: evidence from surface waves. *Geochem. Geophys. Geosyst.* 11 (6).
- Bensen, G.D., Ritzwoller, M.H., Barmin, M.P., Levshin, A.L., Lin, F., Moschetti, M.P., et al., 2007. Processing seismic ambient noise data to obtain reliable broad-band surface wave dispersion measurements. *Geophys. J. Int.* 169 (3), 1239–1260.
- Birch, F., 1943. Elasticity of igneous rocks at high temperatures and pressures. *Geol. Soc. Am. Bull.* 54 (2), 263–286.
- Bjarnason, I.T., Menke, W., Flóvenz, Ó.G., Caress, D., 1993. Tomographic image of the Mid-Atlantic Plate Boundary in southwestern Iceland. *J. Geophys. Res.* 98 (B4), 6607.
- Brandsdóttir, B., Menke, W.H., 1992. Thin low-velocity zone within the Krafla Caldera, NE-Iceland attributed to a small magma chamber. *Geophys. Res. Lett.* 19 (24), 2381–2384.
- Brandsdóttir, B., Menke, W., Einarsson, P., White, R.S., Staples, R.K., 1997. Färoe-Iceland Ridge experiment 2. Crustal structure of the Krafla central volcano. *J. Geophys. Res., Solid Earth* 102 (102), 7867–7886.
- Caricchi, L., Burlini, L., Ulmer, P., 2008. Propagation of P and S-waves in magmas with different crystal contents: insights into the crystallinity of magmatic reservoirs. *J. Volcanol. Geotherm. Res.* 178 (4), 740–750.
- Darbyshire, F.A., Bjarnason, I.T., White, R.S., Flóvenz, Ó.G., 1998. Crustal structure above the Iceland mantle plume imaged by the ICEMELT refraction profile. *Geophys. J. Int.* 135 (3), 1131–1149.
- Darbyshire, F.A., White, R.S., Priestley, K.F., 2000a. Structure of the crust and uppermost mantle of Iceland from a combined seismic and gravity study. *Earth Planet. Sci. Lett.* 181 (3), 409–428.
- Darbyshire, F.A., Priestley, K.F., White, R.S., Stefánsson, R., Gudmundsson, G.B., Jakobsdóttir, S.S., 2000b. Crustal structure of central and northern Iceland from analysis of teleseismic receiver functions. *Geophys. J. Int.* 143 (1), 163–184.
- DeMets, C., Gordon, R.G., Argus, D.F., 2010. Geologically current plate motions. *Geophys. J. Int.* 181 (1), 1–80.
- Dunn, R.A., Forsyth, D.W., 2007. Crust and lithospheric structure – seismic structure of mid-ocean ridges. In: *Treatise of Geophysics*. Elsevier, pp. 419–443.
- Dunn, R.A., Toomey, D.R., Solomon, S.C., 2000. Three-dimensional seismic structure and physical properties of the crust and shallow mantle beneath the East Pacific Rise at 9°30'N. *J. Geophys. Res., Solid Earth* 105 (B10), 23537–23555.
- Dunn, R.A., Lekić, V., Detrick, R.S., Toomey, D.R., 2005. Three-dimensional seismic structure of the Mid-Atlantic Ridge (35°N): evidence for focused melt supply and lower crustal dike injection. *J. Geophys. Res., Solid Earth* 110 (B9).
- Dziewonski, A., Bloch, S., Landisman, M., 1969. A technique for the analysis of transient seismic signals. *Bull. Seismol. Soc. Am.* 59 (1), 427–444.
- Einarsson, P., 1978. S-wave shadows in the Krafla Caldera in NE-Iceland, evidence for a magma chamber in the crust. *Bull. Volcanol.* 41 (3), 187–195.
- Foulger, G.R., Pritchard, M.J., Julian, B.R., Evans, J.R., Allen, R.M., Nolet, G., et al., 2001. Seismic tomography shows that upwelling beneath Iceland is confined to the upper mantle. *Geophys. J. Int.* 146 (2), 504–530.
- Green, R.G., White, R.S., Greenfield, T., 2014. Motion in the north Iceland volcanic rift zone accommodated by bookshelf faulting. *Nat. Geosci.* 7, 29–33.
- Greenfield, T., White, R.S., Roecker, S., 2016. The magmatic plumbing system of the Askja central volcano, Iceland, as imaged by seismic tomography. *J. Geophys. Res., Solid Earth* 121 (10), 7211–7229.
- Gudmundsson, M.T., Larsen, G., 2015. The Grímsvötn volcanic system. *Cat. Icelandic Volcanoes IMO, UI. CPD-NCIP*.
- Gudmundsson, Ó., Brandsdóttir, B., Menke, W., Sigvaldason, G.E., 1994. The crustal magma chamber of the Katla volcano in south Iceland revealed by 2-D seismic undershooting. *Geophys. J. Int.* 119 (1), 277–296.
- Gudmundsson, Ó., Khan, A., Voss, P., 2007. Rayleigh-wave group-velocity of the Icelandic crust from correlation of ambient seismic noise. *Geophys. Res. Lett.* 34 (14), L14314.
- Hammond, J.O.S., Kendall, J.-M., Stuart, G.W., Keir, D., Ebinger, C., Ayele, A., et al., 2011. The nature of the crust beneath the Afar triple junction: evidence from receiver functions. *Geochem. Geophys. Geosyst.* 12 (12).
- Hardarson, B.S., Fitton, J.G., Ellam, R.M., Pringle, M.S., 1997. Rift relocation – a geochemical and geochronological investigation of a palaeo-rift in northwest Iceland. *Earth Planet. Sci. Lett.* 153, 181–196.

- Harmon, N., Rychert, C.A., 2016. Joint inversion of teleseismic and ambient noise Rayleigh waves for phase velocity maps, an application to Iceland. *J. Geophys. Res., Solid Earth* 121.
- Herrmann, R.B., Ammon, C.J., 2004. *Computer Programs in Seismology: Surface Waves, Receiver Functions and Crustal Structure*. Saint Louis University, Saint Louis, MT.
- Hoof, E.E.E., Detrick, R.S., Toomey, D.R., Collins, J.A., Lin, J., 2000. Crustal thickness and structure along three contrasting spreading segments of the Mid-Atlantic Ridge, 33.5°–35°N. *J. Geophys. Res., Solid Earth* 105 (B4), 8205–8226.
- Jóhannesson, H., Saemundsson, K., 1998. *Jardfraedikort af Islandi. Hoggun (Geological Map of Iceland. Tectonics)* (map), Náttúrfraedistofunu Islands, Icelandic Inst. Nat. Hist., Reykjavik.
- Klein, E.M., Langmuir, C.H., 1987. Global correlations of ocean ridge basalt chemistry with axial depth and crustal thickness. *J. Geophys. Res.* 92 (B8), 8089.
- Larsen, G., Gudmundsson, M.T., 2015. The Bárðarbunga volcanic system. *Cat Icelandic Volcanoes IMO. UI, CPD-NCIP*.
- Levshin, A.L., Ritzwoller, M.H., 2001. Automated detection, extraction, and measurement of regional surface waves. *Pure Appl. Geophys.* 158 (8), 1531–1545.
- Li, A., Detrick, R.S., 2006. Seismic structure of Iceland from Rayleigh wave inversions and geodynamic implications. *Earth Planet. Sci. Lett.* 241, 901–912.
- Matthews, S., Shorttle, O., MacLennan, J., 2016. The temperature of the Icelandic mantle from olivine-spinel aluminum exchange thermometry. *Geochem. Geophys. Geosyst.* 17 (11), 4725–4752.
- Menke, W., Brandsdóttir, B., Einarsson, P., Bjarnason, I.T., 1996. Reinterpretation of the RRISP-77 Iceland shear-wave profiles. *Geophys. J. Int.* 126 (1), 166–172.
- Menke, W., West, M., Brandsdóttir, B., Sparks, D., 1998. Compressional and shear velocity structure of the lithosphere in northern Iceland. *Bull. Seismol. Soc. Am.* 88 (6), 1561–1571.
- Mitra, S., Priestley, K., Gaur, V.K., Rai, S.S., Haines, J., 2006. Variation of Rayleigh wave group velocity dispersion and seismic heterogeneity of the Indian crust and uppermost mantle. *Geophys. J. Int.* 164 (1), 88–98.
- Rickers, F., Fichtner, A., Trampert, J., 2013. The Iceland–Jan Mayen plume system and its impact on mantle dynamics in the North Atlantic region: evidence from full-waveform inversion. *Earth Planet. Sci. Lett.* 367, 39–51.
- Schuler, J., Greenfield, T., White, R.S., Roecker, S.W., Brandsdóttir, B., Stock, J.M., et al., 2015. Seismic imaging of the shallow crust beneath the Krafla central volcano, NE Iceland. *J. Geophys. Res., Solid Earth* 120 (10), 7156–7173.
- Shapiro, N.M., Campillo, M., 2004. Emergence of broadband Rayleigh waves from correlations of the ambient seismic noise. *Geophys. Res. Lett.* 31 (7).
- Shapiro, N.M., Campillo, M., Stehly, L., Ritzwoller, M.H., 2005. High-resolution surface-wave tomography from ambient seismic noise. *Science* 307 (5715), 1615–1618.
- Shorttle, O., MacLennan, J., 2011. Compositional trends of Icelandic basalts: implications for short-length scale lithological heterogeneity in mantle plumes. *Geochem. Geophys. Geosyst.* 12, Q11008.
- Sigvaldason, G.E., Steinthorsson, S., Oskarsson, N., Imsland, P., 1974. Compositional variation in recent Icelandic tholeiites and the Kverkfjöll hot spot. *Nature* 251 (5476), 579–582.
- Staples, R.K., White, R.S., Brandsdóttir, B., Menke, W., Maguire, P.K.H., McBride, J.H., 1997. Färoe–Iceland Ridge experiment 1. Crustal structure of northeastern Iceland. *J. Geophys. Res., Solid Earth* 102 (B4), 7849–7866.
- White, R., McKenzie, D., 1989. Magmatism at rift zones: the generation of volcanic continental margins and flood basalts. *J. Geophys. Res.* 94 (B6), 7685.
- White, R.S., McKenzie, D., O’Nions, R.K., 1992. Oceanic crustal thickness from seismic measurements and rare earth element inversions. *J. Geophys. Res.* 97 (B13), 715.
- Wolfe, C.J., Bjarnason, I.Th., VanDecar, J.C., Solomon, S.C., 1997. Seismic structure of the Iceland mantle plume. *Nature* 385 (6613), 245–247.